PSFC/JA-06-28

Comparison of solid and plasma linear energy deposition for electron preheat and fast ignition scenarios

Chen, C.D., Li, C.K., and Petrasso, R.D.*

* Also Visiting Senior Scientist, Laboratory for Laser Energetics, University of Rochester

November
2006

Plasma Science and Fusion Center
Massachusetts Institute of Technology
Cambridge MA 02139 USA

Comparison of solid and plasma linear energy deposition for electron preheat and fast ignition scenarios

C.D. Chen, C.K. Li, and R.D. Petrasso[*]
Plasma Science Fusion Center, Massachusetts Institute of Technology
Fusion Science Center
Cambridge, MA 02139, USA

Abstract

Fast electron transport has been examined in the single particle regime in cold matter and in a fully ionized, classical cold plasma of solid-density using the Monte Carlo code ITS 3.0 and the CELSA plasma model by Li and Petrasso. Primary electron penetration in DT ice has been found to be ~40% larger than in a DT plasma of equivalent density. This is attributed primarily to the plasma wave contribution to the plasma stopping power. Scattering is quantified by range straggling and lateral blooming; its ratio to penetration was found comparable in DT plasma and ice. Similar trends are found for higher Z materials, though direct quantitative comparison requires a to-be-performed normalization of the outputs of the two models and an inclusion of radiative effects in the plasma model.

Introduction

Electron transport and energy deposition are topics that have been extensively studied over the past century[1], especially in cold matter, where the effects of energy loss and scattering have been well characterized, and where the physical processes have been implemented in a number of different transport codes. Specifically, in the single particle regime, some of the more widely used Monte Carlo codes include ITS[2], Geant4[3], EGS[4], and Penelope[5], among others. In the context of inertial fusion, accurate calculation of the energy deposition profile from fast electrons and from radiation is important for discerning the conditions under which an implosion will fail. Energetic electrons, however, have different roles and consequences in the contexts of the two most widely discussed scenarios for inertial fusion, namely hot spot fusion and fast ignition[6]. For hot spot fusion, energetic electrons of 10-100 keV[7] that penetrate and interact with the DT fuel can adversely raise the fuel temperature (equivalently the adiabat) [8], thereby precluding adequate compression and ignition. In treating this case, the electrons are usually propagated through a dense (~1 g/cc) cool plasma, though this is sometimes approximated as cold DT matter.

In contrast, for fast ignition, energetic (~1 MeV) electrons, generated from intense laser-plasma interactions, are required to penetrate far enough into the core of the imploded target to deposit their energy locally and ignite the ultra-dense (~300 g/cc) DT plasma. Despite the importance of the plasma regime in either the hot spot or fast ignition scenarios, workers sometimes approximate energy deposition with cold matter models due to the convenience and prevalence of the computational tools available. Thus, in this paper we seek to understand and delineate the differences in fast electron transport between the cold matter and plasma regimes in order to better understand where this approximation is valid and where it breaks down.

While electron scattering and energy loss are well characterized in solids, they are not as well understood in plasmas. Recently, an analytic electron transport model has

been developed by Li and Petrasso that couples the energy loss in plasmas to coulomb scattering through a diffusion equation[9]. The CELSA model (Coupled Energy Loss and Scattering Approximation) uses moments of the diffusion equation to calculate the mean penetration, range straggling, and lateral blooming of relativistic electrons propagated through a cold, fully ionized classical plasma.

In this paper we used the ITS 3.0 Monte Carlo code to represent transport through cold matter, and compared the results to predictions of the CELSA model for fully ionized, classical cold plasmas. We have used these calculations to study electron transport trends in both the initial energy and the atomic composition of the medium. In part II of this paper we contrast the differences between solid and plasma energy loss along a path, through use of the straight-line continuous slowing down approximation (CSDA), which is tabulated by Berger and Seltzer[10]. In parts III and IV we add in the effects of scattering and examine the linear energy transfer, scattering, and blooming in the two regimes. Appendix A at the end addresses validation of the ITS 3.0 code system through comparisons previous validation efforts and other experimental data published in the literature. It also has a short discussion on the definition of range and path length and the importance of scattering for cold matter.

Energy Loss Rates

We first take a look at the differences between the plasma and cold matter straight-line stopping powers. Here, for cold matter, we use the stopping power from the NIST ESTAR database[11], whose underlying physics includes collisional stopping powers from Bethe[12] with Sternheimer's density-effect correction[13] and, in our energy regime, radiative stopping powers from interpolations by Pratt[14]. Shell corrections are not included in the ESTAR database and thus reduce the accuracy below 1 keV. For cold matter, the total stopping power is thus given by

$$\left(-\frac{dE}{ds}\right)_{total} = \left(-\frac{dE}{ds}\right)_c + \left(-\frac{dE}{ds}\right)_r$$

where the analytic form of the collisional stopping power is

$$\left(-\frac{dE}{ds}\right)_c = \frac{2\pi r_0^2 m_e c^2 n_i Z}{\beta^2}\left[\ln\left(\frac{m_e c^2 \gamma^2 \beta^2 T}{2I^2}\right) - \ln(2)\left(\frac{2}{\gamma}-1+\beta^2\right) + \frac{1}{\gamma^2} + \frac{\left(1-\frac{1}{\gamma}\right)^2}{8} - \delta\right]$$

Here, dE/ds represents energy loss along a particle path. In cold matter, the collisional energy loss is due to inelastic Coulomb collisions with the atomic electrons. Bethe's derivation makes use of the Møller cross section for electron-electron scattering, and thus includes relativity and quantum mechanical effects. The δ function above represents the density-effect correction. The radiative stopping power is due to bremsstrahlung emission in the medium.

In a cold, fully-ionized classical plasma, we follow the CELSA model from Li and Petrasso and take the stopping power as

$$\left(-\frac{dE}{ds}\right) = \frac{2\pi r_0^2 m_e c^2 n_i Z}{\beta^2}\left[\ln\left(\frac{(\gamma-1)\lambda_D}{2\sqrt{2\gamma}r_0}\right)^2 + 1 + \frac{\left(1-\frac{1}{\gamma}\right)^2}{8} - \ln(2)\left(2-\frac{1}{\gamma}\right) + \ln\left(\frac{1.123\beta}{\sqrt{2kT_e/m_e c^2}}\right)^2\right]$$

where binary collisions and plasma oscillations are included but not bremsstrahlung. For the binary collisions we again use Møller scattering with the maximum energy loss as ½ the kinetic energy for indistinguishable particles, but this time with the minimum energy transfer taken at the Debye length. The last term represents the contribution to the energy loss from plasma oscillations. We note that in this first approximation to the plasma stopping power, the temperature dependence in the various terms cancels out. Thus, the model assumes a plasma temperature where the plasma is fully ionized, but low (cold) relative to the incident particle energy.

In Figure 1 we compare the stopping power of a 50-50 mix of DT ice at solid density to that of a fully ionized plasma at the same density. We see that in this model, the stopping power in cold matter is consistently lower than that in the plasma across a large energy spectrum. Figure 3 shows the exact plasma/solid stopping ratio, and we see that it is roughly 40% for lower energy incident particles. This difference in stopping power is due to the wave oscillations in the cold plasma. Additionally, the DT stopping ratio starts to fall off above a few hundred keV in Figure 3. This is due primarily to 2 factors: the reduced sensitivity to differences in the solid/plasma medium from the higher energy particle and, to a much lesser extent in DT, the neglect of bremsstrahlung radiation in the plasma model. We see bremsstrahlung start to come into play only slightly in Figure 1 above a few hundred keV, as the cold matter stopping power begins to rise slightly toward the plasma stopping power. The neglect of bremsstrahlung radiation plays a larger role in higher Z materials, and thus we do not plot the stopping power ratio for beryllium and copper above 1 MeV in Figure 3.

Figure 2 examines the stopping powers for beryllium, aluminum, and copper. These materials were chosen to give a representative sample of materials relevant to ICF across a range of atomic numbers. Because of its absorption abilities, beryllium is currently the ablator of choice for the NIF indirect drive point design[15]. Copper is used to dope the beryllium ablator in order to improve the absorption of x-rays and thus increase capsule performance[16]. Aluminum was chosen as a midpoint between these atomic numbers and was benchmarked to experimental data compiled by Evans[17]. We again assume a plasma temperature sufficiently high for full ionization, but cold relative to the incident electron energy. We see in Figure 3 that the plasma stopping power is significantly higher than in the solid case. The plasma waves contribute the entire difference, while the decline in the ratio is due to the reduced sensitivity to the medium as the incident particle energy increases, and, for higher Z materials above a few hundred keV, the absence of bremsstrahlung in the plasma. The copper stopping power ratio is higher because the higher average ionization energy results in a lower stopping power in the solid.

In Figure 4 we examine the density dependence of the stopping power, using solid and gaseous DT densities for cold matter and a solid-density and a compressed, 300 g/cc density for the DT plasma. We see that the gas- and solid-density cold matter cases are the same for much of the energy range, diverging slightly above 1 MeV. The stopping power in DT ice is lower than in the gaseous DT (when normalized to density) because the density-effect correction starts to come into play. The stopping power for the two solid-density and compressed-density plasmas, however, is rather different, owing to the difference in the Debye length in the coulomb logarithm of the collision term. This reduces the number of collisions in the plasma, thus resulting in a lower stopping power

for the higher density plasma. We also note that fortuitously, the stopping power of the 300 g/cm^3 DT plasma comes out to be the same as that of the DT ice.

Qualitative Effects of Scattering

While stopping powers provide information on particle energy loss along a given path length, the actual energy deposition profile within a volume is altered by scattering[18]. Since, apart from an insensitive dependence on the coulomb logarithm the scattering mechanism is the same in both plasmas and in cold matter[19], we first review the qualitative effects of scattering in cold matter before examining the differences between the two states. Cold matter scattering simulations were performed with the Monte Carlo code ITS 3.0. A thin beam of 1 MeV electrons was injected into various materials and the primary electrons (the higher energy electron in a collision) were tracked to their endpoint positions. The endpoints of the secondary electrons were ignored in order to directly compare results to the CELSA model predictions. The energy deposition by secondary electrons is included in energy deposition profiles, which are necessary for future work.

Figure 5 provides a pictorial representation of these endpoints for DT, Be, Al, Cu, and Au. All five figures are on the same scale in units of areal density, and the dashed line represents the CSDA range. Here we see a qualitative change in scattering as the atomic number increases**.** Penetration into the material varies inversely with atomic number, even when considered in units of areal density. As the atomic number increases, we also see the effects of scattering become more pronounced, leading to a "rounder" shape for higher Z materials. Therefore, for higher Z materials, the increased scattering results in a faster randomization of the directionality of the beam. We define range straggling and lateral blooming as the standard deviations of the primary electron endpoints when taken to zero energy

$$\Sigma_R(E) = \sqrt{\langle x^2 \rangle - \langle x \rangle^2} \qquad \qquad \Sigma_B(E) = \sqrt{\langle y^2 \rangle}$$

where the x axis is perpendicular to the surface and into the material (with the origin at the point the beam enters the material) and the y axis is any direction tangential to the surface, since we assume cylindrical symmetry. We note that quantitative values for penetration, straggling, and blooming in cold matter for these materials are given in Figure 10.

Figure 6 shows the primary electron endpoints for beams of varying energy into DT ice. While the magnitude of the penetration, blooming, and straggling vary by a factor of 10 between each picture, we note that the qualitative nature of the scattering is nearly identical for different input energies into DT. This is only approximately true; as later seen in Figures 8 and 9 there is a slight quantitative difference at higher beam energies. In a pictorial representation, however, it is not discernable. This will not be true if the beam energy gets high enough that radiative effects become important. For DT this occurs at relatively high energies that are not as relevant to preheat and fast ignition scenarios. For higher Z materials, radiative effects will come into play at fast ignition energies.

Stopping, Straggling, and Blooming

Mean penetration, range straggling, and lateral blooming have been calculated using ITS Monte Carlo simulations for cold matter (as shown in the previous section) and the CELSA model for cold, fully ionized classical plasmas. There are slight differences in the outputs of the two models, and as such, we need to be careful in our comparisons. The ITS simulation is a condensed history Monte Carlo model where primary electrons are scattered in steps and lose energy until they reach a specified cutoff energy, where they then continuously lose the remainder of their energy without scattering. In the CELSA model, the electron endpoint is taken to be where the electron has lost its directionality, characterized by the energy at which $<\cos\theta>=1/e$. For Z=1, the two energy endpoints are nearly identical since the collisional energy loss rate and the momentum loss rate are of the same order. For higher Z materials there is significantly more scattering, and the primary electron endpoint energy where loss of directionality occurs is a considerable fraction of the initial energy. Thus, we only perform a direct quantitative comparison of mean penetration, straggling, and blooming for the Z=1 case. For higher Z materials we will only examine similarities in the relevant trends.

Figure 7 shows the mean penetration of electrons into 50-50 DT ice and into a fully ionized, classical cold DT plasma at solid density. The data is tabulated below the figure. We see that the mean penetration is up to 40% higher in the cold matter case. The difference then falls slowly for a relatively wide energy range. This difference is most likely explained by the difference in the stopping powers, which also exhibits about a 40% stronger stopping in the plasma. At higher energies this difference falls off both due to the reduced sensitivity of a higher energy particle to the structure of the medium, and to the effect of neglecting the bremsstrahlung in the CELSA model. Quantifying the relative contributions of the two effects would require including bremsstrahlung effects in the CELSA model, which one would seek to do in future work.

Figures 8 and 9 compare the range straggling and lateral blooming of the primary electrons in the DT ice and solid-density DT plasma cases. We see that since they are normalized to the mean penetration, the differences in the stopping power are factored out and the solid and plasma cases are nearly identical. Thus for Z=1, the effects of scattering are the same in both the plasma and solid cases. Also, the straggling and blooming ratios are relatively flat up to 1 MeV, suggesting that the shape of the spatial electron distribution stays relatively fixed up to this energy, as depicted in Figure 6. This is likely because both the amount of blooming and the actual penetration are proportionate to the degree of scattering and the energy loss rate. The discrepancy above 1 MeV in the range straggling is most likely due to zoning effects in our simulations.

Figure 10 quantifies the penetration, straggling, and blooming that were depicted in Figure 5. Again, for higher atomic numbers, we see an increase in the scattering and a corresponding decrease in the penetration, even when the penetration is normalized to the density. The straggling and blooming ratios also rise with increasing atomic number, leading to the more "rounded" spatial profiles seen in Figure 5. The straggling and blooming ratios approach a limiting value at high atomic numbers as the electrons rapidly lose their directionality. We see in Figure 11 that the penetration, straggling, and blooming trends in the plasma are very similar to those in the cold matter case, with the drop off in penetration and the rise and saturation of the straggling and blooming ratios.

Conclusions and Future Work

Preliminary work has been performed in studying electron transport in a single particle regime. Transport through cold matter has been compared to transport through a fully ionized, classical cold plasma, and many similar trends have been found to apply. For hydrogenic materials (DT) we quantitatively compare the two models and find that the difference in the penetration is primarily accounted for by the energy loss due to plasma waves. For higher Z materials we also find that the difference in the stopping powers is primarily accounted for by the wave contribution; including bremsstrahlung effects in the plasma model would allow for a more direct comparison at higher incident electron energies (above a few hundred keV). However, since the two transport models output different results, we do not directly compare them to examine differences in scattering for higher Z materials. Not including radiative effects in the plasma model limits the applicability of our results to below ~1 MeV.

In addition to including radiative effects and normalizing the output of the two models, future work would involve taking the outputs of these models and using realistic electron source profiles to study the effects of scattering on the energy deposition and consequent change in adiabat of a given target. This would allow one to compare how the cold matter and plasma models affect the ignition constraints in both preheat and fast ignition scenarios.
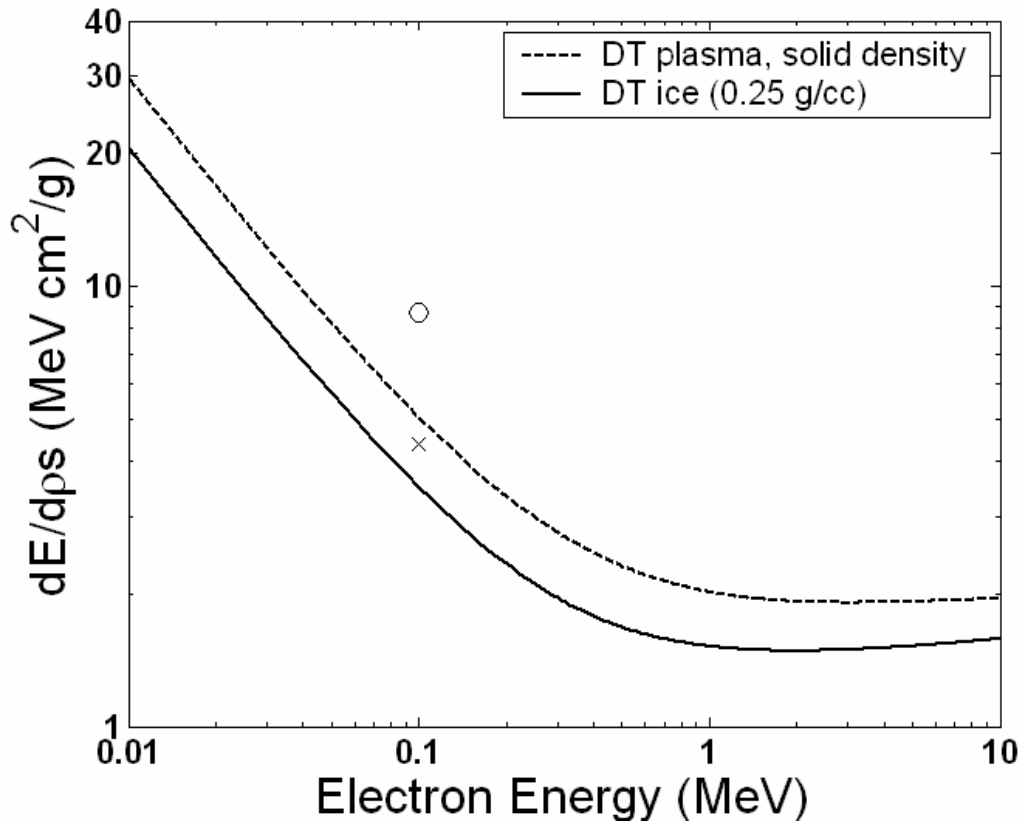
Figures

Figure 1. Stopping powers of 50-50 DT ice and a cold, fully ionized classical DT plasma. We see that the cold matter stopping power is consistently ~40% lower across a wide energy range. Stopping powers shown here can be translated to solid D_2 or solid H_2 by multiplying the stopping power by the respective 1.25 and 2.5 mass factors (as shown by the x and the o points for D_2 and H_2 ice).
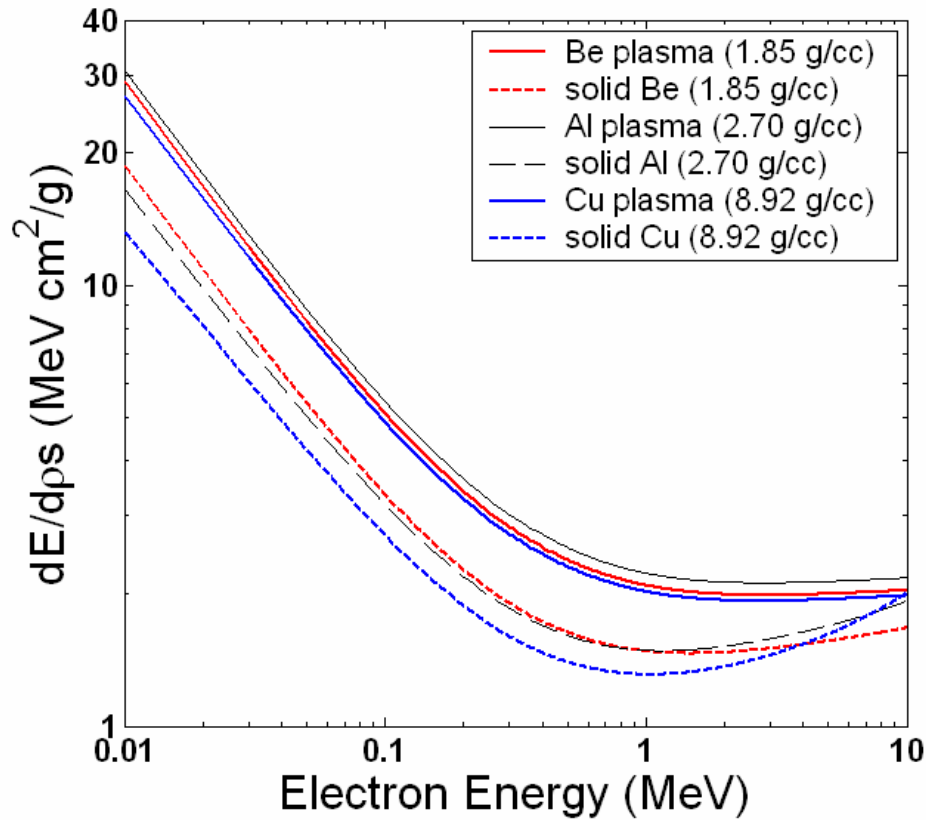
Figure 2. Stopping powers of higher Z plasmas differ more strongly from their cold matter values. The stopping powers are all higher in the respective plasma models. This is again primarily attributable to the plasma wave contribution. The discrepancy at energies greater than a few hundred keV is due to the onset of radiative effects which are not included in the plasma model.
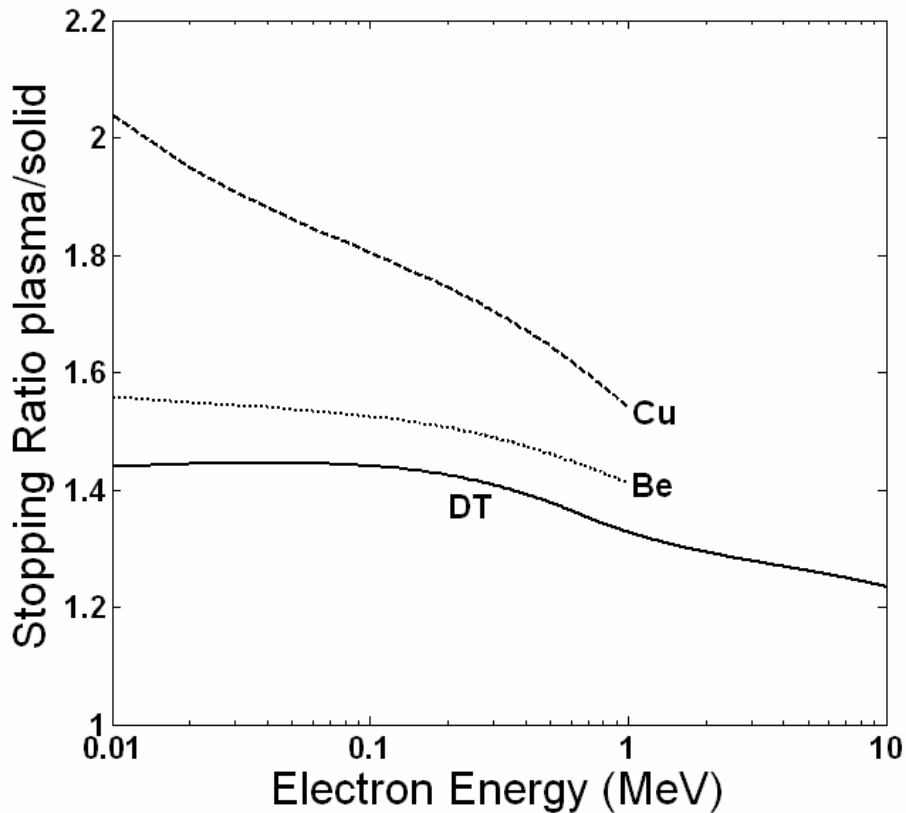
Figure 3. Stopping power ratios for solid-density DT, Be, and Cu. The plasma stopping power is higher than the cold matter stopping power, and attributable to the plasma wave component. As expected, the ratio falls with increasing energy due to both the incident particle becoming less sensitive to its medium and the absence of bremsstrahlung in the plasma model. The absence of radiative effects plays a larger role for higher Z materials and energies above a few hundred keV. The copper stopping power ratio is higher because the higher average ionization energy results in a lower stopping power in the solid.
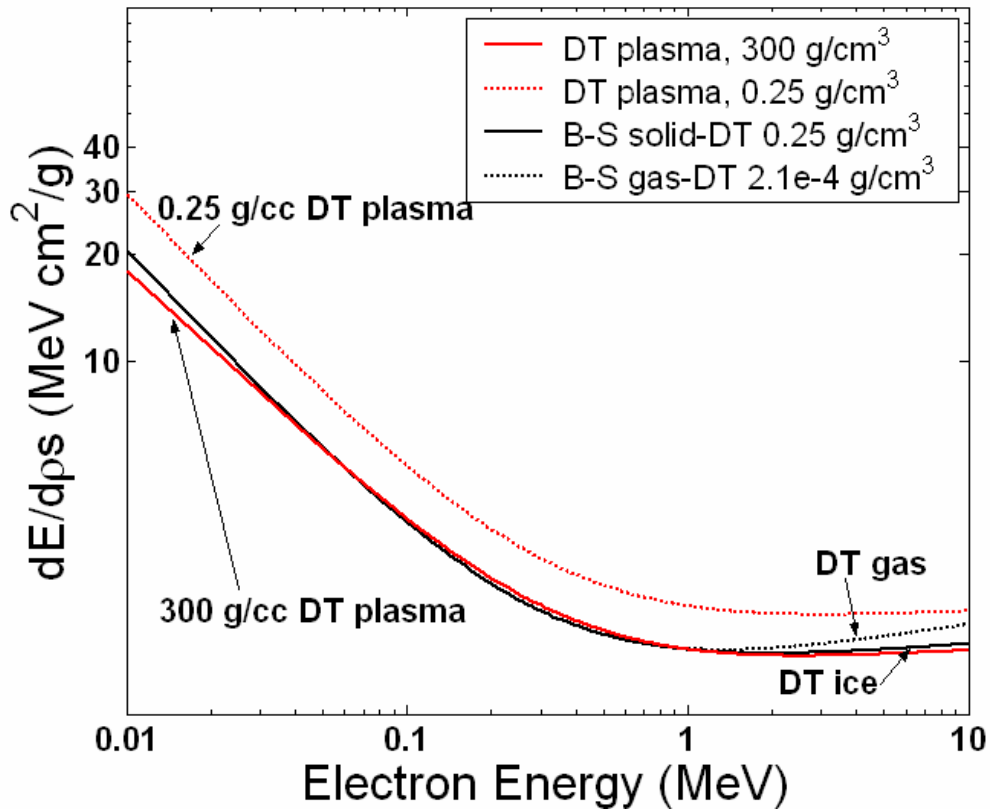
Figure 4. The stopping power in cold matter is similar for the solid and gas densities, diverging slightly at higher energies due to the density-effect correction. The plasma stopping power differs for the different densities. With a smaller debye length in the higher density plasma, the number of collisions is reduced, lowering the stopping power. We also note that fortuitously, the stopping power of a 300 g/cm^{3} DT plasma is very similar to that of the DT ice.
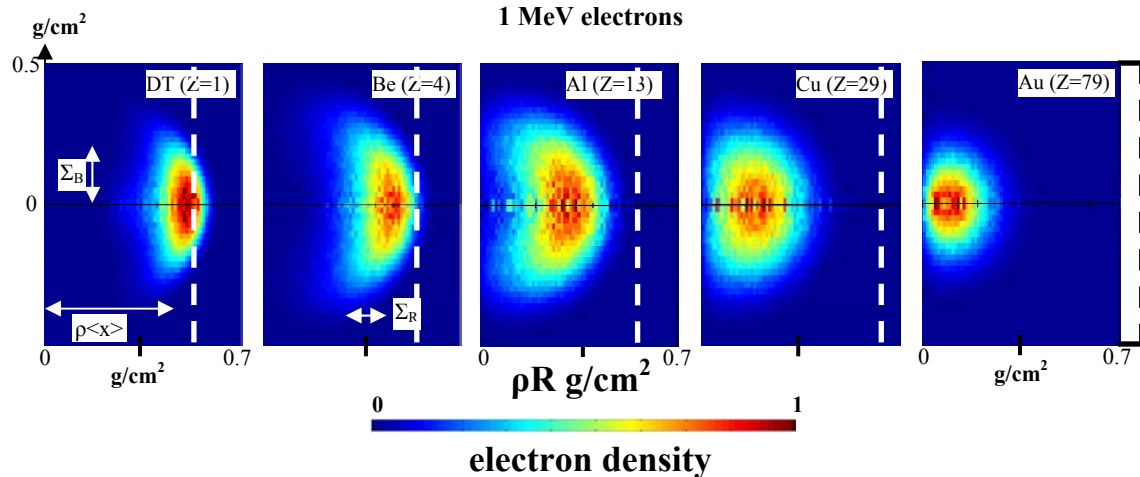
Figure 5. Pictorial representations of the primary electron endpoint of a 1 MeV beam into DT, Be, Al, Cu, and Au. As expected, the qualitative effects of scattering become more pronounced for higher Z materials, leading to a "rounder" shape in the electron endpoint. Penetration decreases with increasing Z, even when considered in units of areal density. Here, the dashed lines represent the ranges from the straight-line continuous slowing down approximation (CSDA range), which is tabulated by Berger and Seltzer. Figure 10 provides quantitative values for the range, straggling, and blooming for 1 MeV electrons into different materials.
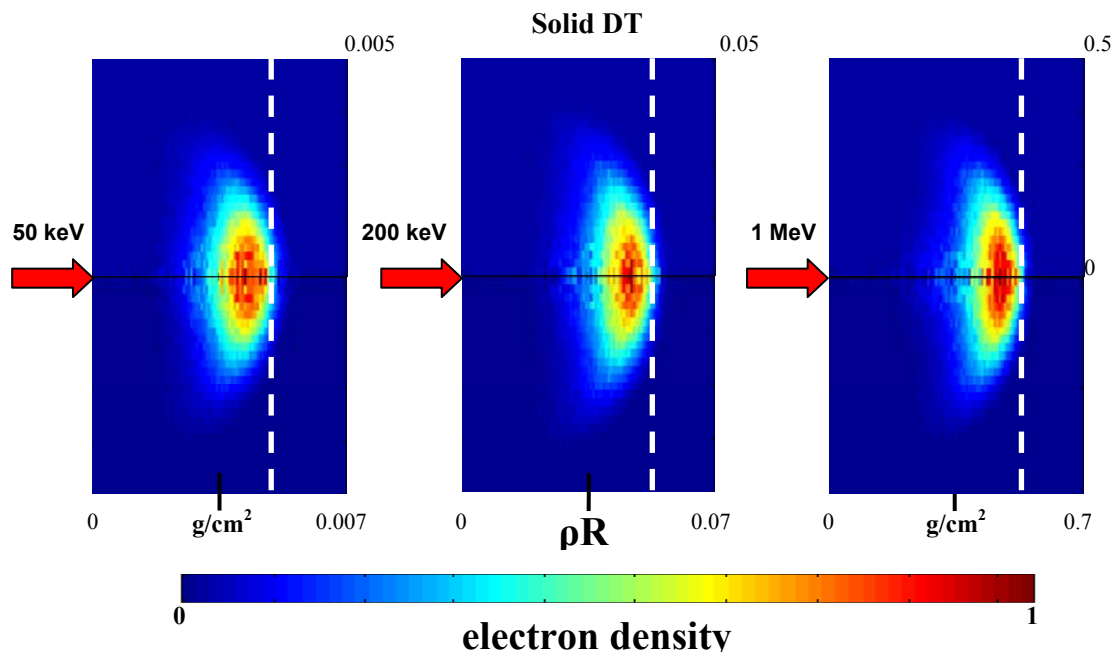

Figure 6. Pictorial representations of electron endpoints for input beams of varying energies into DT. Unlike proton beams which have very little scattering in hydrogenic materials, electron beams are strongly scattered. Note that the areal density scales change by a factor of 10 between each picture. The straggling and blooming ratios only slightly

11

depend on the beam energy for this range of energies. This difference is not discernable in a pictorial representation but quantitative trends are shown in Figures 8 and 9. Again, the dashed lines represent the CSDA range.
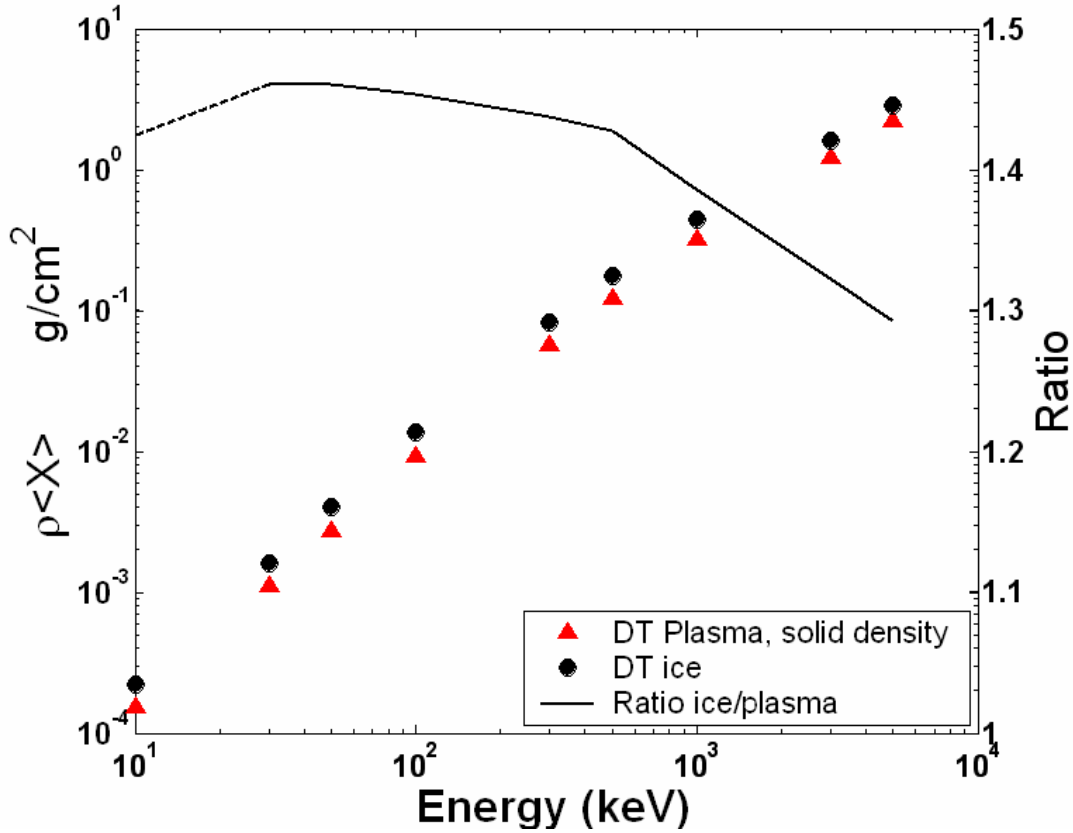
Energy (keV)	10	30	50	100	300	500	1000	3000	5000
Plasma $\rho<x>$ g/cm^2	1.5e-4	1.1e-3	2.8e-3	9.3e-3	5.7e-2	1.2e-1	3.2e-1	1.2	2.2
Cold Matter $\rho<x>$ g/cm^2	2.2e-4	1.6e-3	4.0e-3	1.4e-2	8.2e-2	1.7e-1	4.4e-1	1.6	2.8

Figure 7. Mean penetration of electrons in solid density DT. The penetration in cold matter is about 40% higher than in plasmas, due primarily to the plasma wave contribution to the stopping power. This falls off above several hundred keV as the incident particle becomes less sensitive to the medium and radiative effects start to come into play. The dip in the ratio at l0 keV is due to uncertainties in ITS at that energy.
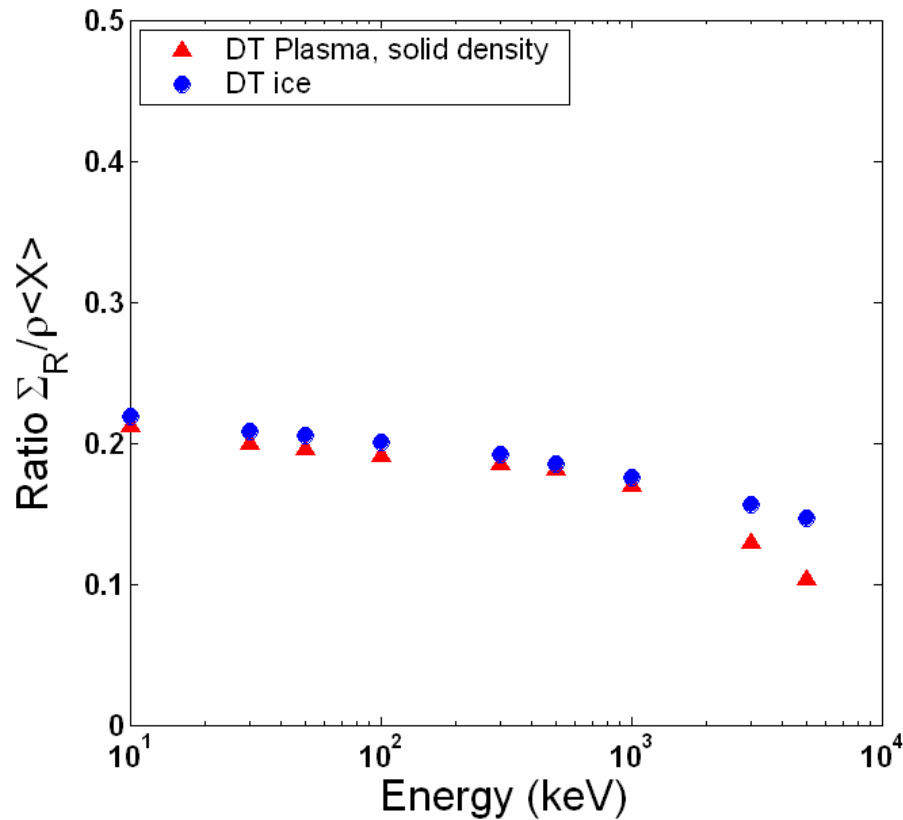
Figure 8. Straggling Ratio for solid density DT. The plasma ratio tracks the cold matter ratio closely for Z=1, suggesting that the scattering is insensitive to the coulomb logarithm. The discrepancies at high energy are likely due to zoning effects in the Monte Carlo simulation.
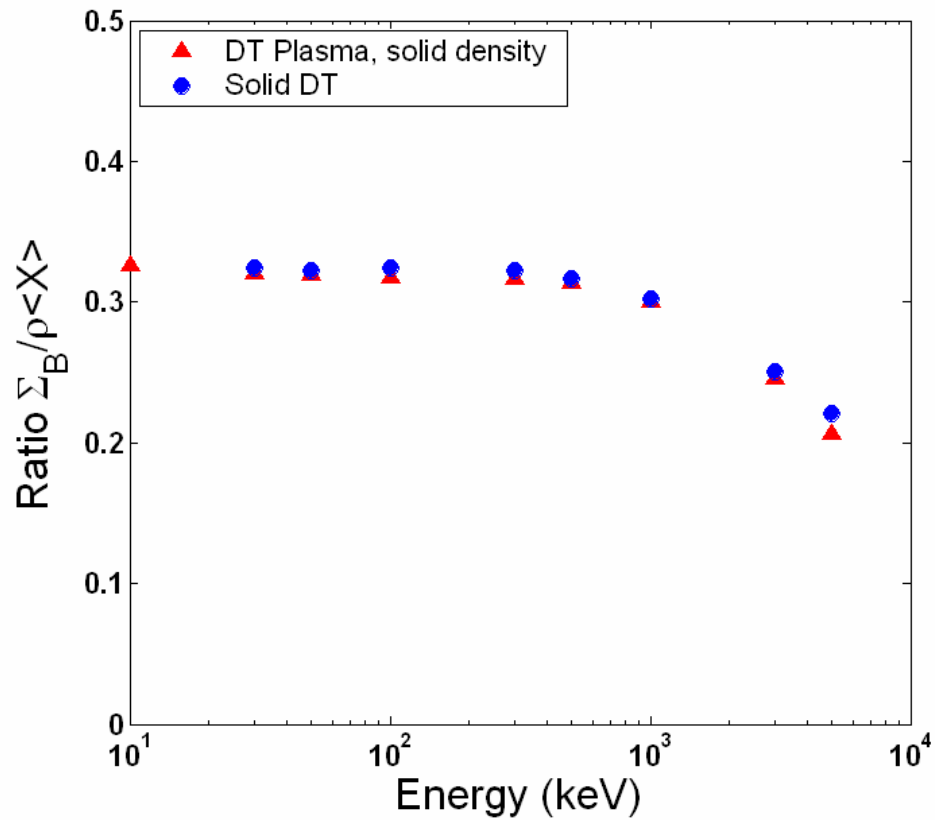
Figure 9. Blooming ratio for DT. Again, the plasma ratio and cold matter ratios are similar, suggesting similarities in the scattering mechanism. The plasma tracks the solid case for a broad range of energies.
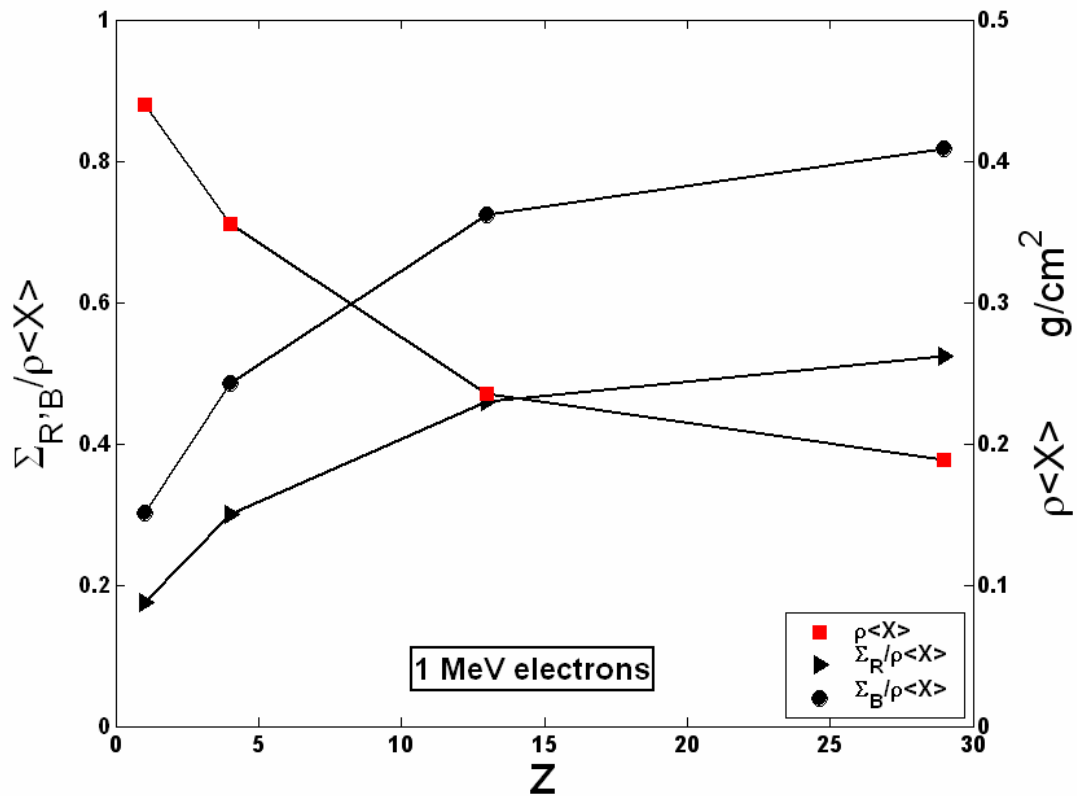
Figure 10. Penetration, straggling, and blooming as a function of atomic number in cold matter for 1 MeV incident electrons. For higher atomic numbers, we see an increase in the scattering and a corresponding decrease in the penetration, even when the penetration is normalized to the density. The straggling and blooming ratios also rise with increasing atomic number, leading to the more "rounded" spatial profiles seen in Figure 5. The straggling and blooming ratios approach a limiting value at high atomic numbers as the electrons rapidly lose their directionality.
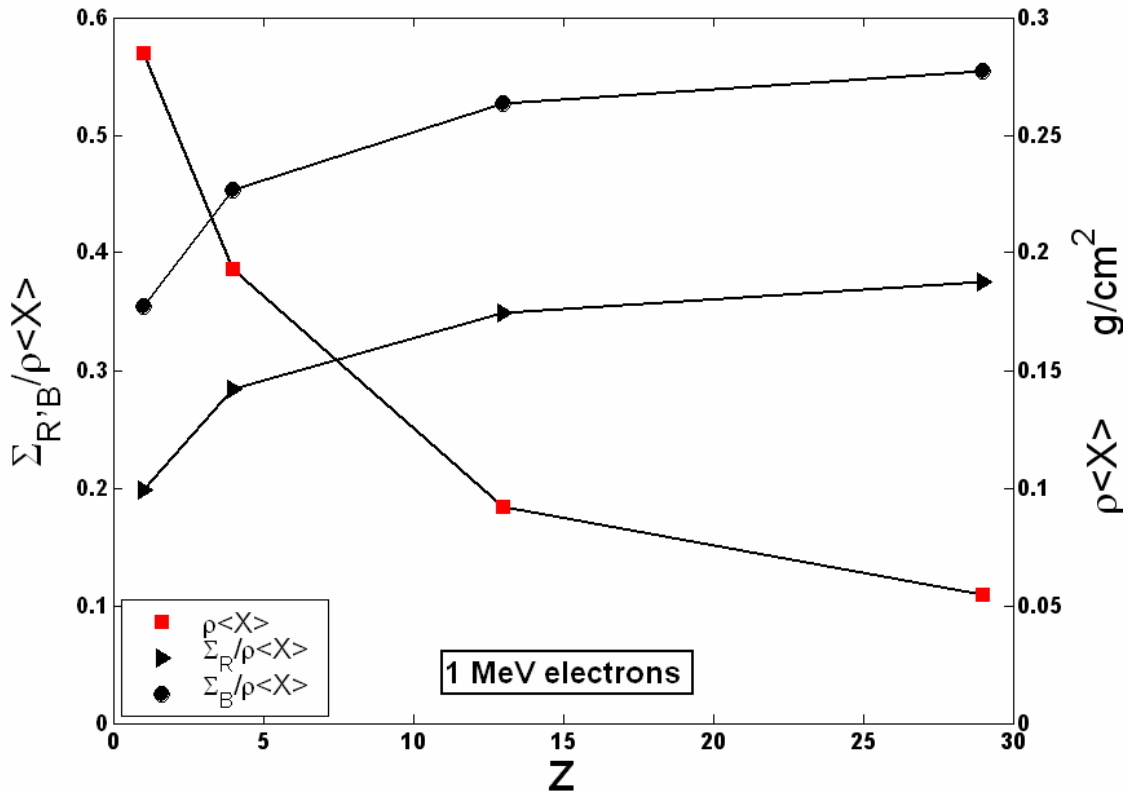
Figure 11. Penetration, straggling, and blooming as a function of atomic number in fully ionized plasmas at solid density for 1 MeV incident electrons. We see very similar trends to the cold matter case, with increased scattering leading to a drop off in penetration, and corresponding rise in straggling and blooming.

[*] Also Visiting Senior Scientist, Laboratory for Laser Energetics, University of Rochester

[1] H. Bethe, Z. Physik 76 293 (1932); R.M. Sternheimer, S.M. Seltzer, and M.J. Berger, Phys. Rev. B**26**, 6067 (1982); S.M. Seltzer and M.J. Berger, Nucl. Instr. Meth. **B12**, 95 (1985)

[2] J.A. Halbleib, R.P. Kensek, T.A. Mehlhorn, G.D. Valdez, S.M. Seltzer, and M.J. Berger, "ITS Version 3.0: The integrated TIGER Series of Coupled Electron/Photon Monte Carlo Transport Codes," Technical Report SAND91-1634, Sandia National Laboratories, 1992

[3] S. Agostinelli et al., Nuclear Instruments and Methods **A** 506 (2003) 250-303

[4] I. Kawrakow and D.W.O. Rogers, "The EGSnrc Code System: Monte Carlo Simulation of Electron and Photon Transport", NRCC Report PIRS-701, National Research Council of Canada, 2003

[5] F. Salvat, J.M. Fernandez-Varea, E. Acosta, and J. Sempau, "PENELOPE, A Code System for Monte Carlo Simulation of Electron and Photon Transport", Proceedings of a Workshop/Training Course, OECD/NEA 5-7 November 2001, NEA/NSC/DOC(2001)19. ISBN: 92-64-18475-9

[6] M. Tabak, *et. al.*, Phys. Plasmas **1**, 1626 (1994)

[7] K. Mima, *et. al.*, *Laser and Particle Beams*, v 7, pt.3, Aug. 1989, 487-93

[8] B. Yaakobi, et.al., Phys. Plasmas **7**, 3714 (2000)

[9] C.K. Li and R.D. Petrasso, Phys. Rev. E **73**, 016402 (2006)

[10] S.M. Seltzer and M.J. Berger, International Journal of Applied Radiation and Isotopes, **35**, 665 (1984)

[11] http://physics.nist.gov/PhysRefData/Star/Text/ESTAR.html

[12] Bethe H 1932 Z. Physik 76 293

[13] Sternheimer, R. M., Phys. Rev. **88**, 851 (1952)

[14] Pratt, R. H., et. al., Atomic Data Nucl. Data Tables **20**, 175.(1977)

[15] J.D. Lindl, Phys. Plasmas 2, 3933 (1995).

[16] D.C. Wilson, *et. al.*, The development and advantages of beryllium capsules for the National Ignition Facility, 39th Annual Meeting of the Division of Plasma Physics of the American Physical Society. Invited and Review Papers, 17-21 Nov. 1997 , Pittsburgh, PA, USA

[17] R.D. Evans, *The Atomic Nucleus* (Krieger Publishing Company, 1982).

[18] H. H. Hubbel *et al.*, Phys. Rev. A **26**, 2460 (1982).

[19] B. Trubnikov, *Review of Plasma Physics 1* (Consultants Bureau, New York, 1965).

Appendix A-Validation of ITS

The Integrated Tiger Series, version 3.0 is an established Monte Carlo code system used for coupled electron-photon transport and has been employed for a number of years in fields ranging from medical physics to nuclear shielding calculations. It has been well benchmarked against a variety of target materials and for a wide range of energies, from a few tens of keV to hundreds of MeV for materials from Beryllium to Uranium[123]. In order to verify our implementation of the ITS 3.0 code, we benchmarked our results to experimental "extrapolated range" data for aluminum collected by Evans[4], and originally measured by Schonland[5] and Varder[6]. Here, following Evans, we compare the extrapolated range to the experimental data. This differs from the mean range that we use in the main text. The extrapolated range takes the slope of the cumulative distribution function of the transmitted electrons at the median and extrapolates the distance to zero transmission. This is shown in Figure A1.

Figure A2 shows our extrapolated range calculations in aluminum for the energies of interest in this paper. These are compared to the experimental data and the Berger-Seltzer Continuous Slowing Down Approximation range (average total path length). We see that there is a good match between the ITS 3.0 extrapolated range calculations in aluminum and the experimental data. Figure A3 provides ITS extrapolated range calculations for beryllium and gold and compares them to experimental data from Tabata (ref. 2) and the CSDA range. We see that there is a good match up of ITS to the experimental data. We also note that for lower Z materials, as scattering becomes less important, the extrapolated range approaches the CSDA range. The mean range which we quote in the text, however, is shorter than the extrapolated range and the CSDA range (as seen in Fig. 5), even for hydrogenic materials.

Figure A4 compares the ratios of the extrapolated range to Berger-Seltzer, and the mean range to Berger-Seltzer for DT, beryllium, aluminum, copper, and gold. We can see the increase in the importance of scattering as the mean and extrapolated range to CSDA ratios decrease for higher Z materials. We also see the reduced sensitivity to scattering for higher energy particles. The dip above 1 for Z=1 is probably due to small errors introduced into the linear interpolation of the extrapolated range.
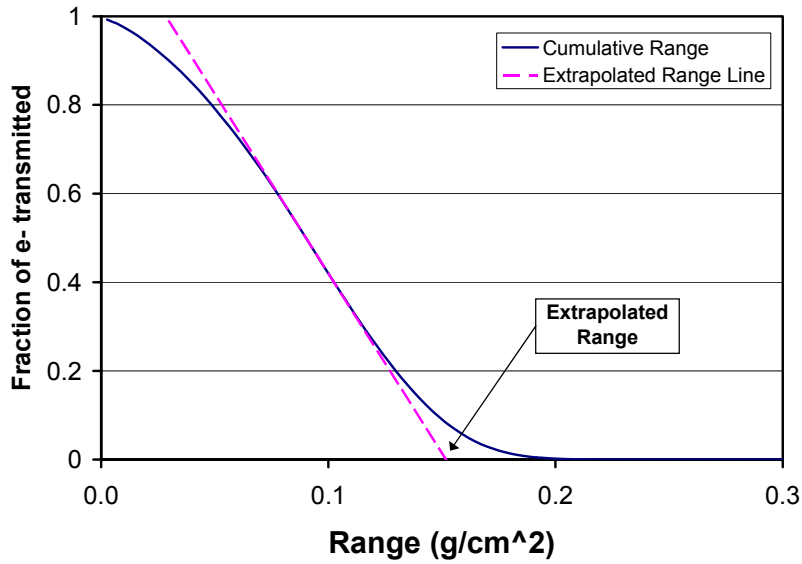
Fig. A1. The extrapolated range is defined as the location where the line defined by the slope of the cumulative distribution function at and tangent to the median point hits the x axis.
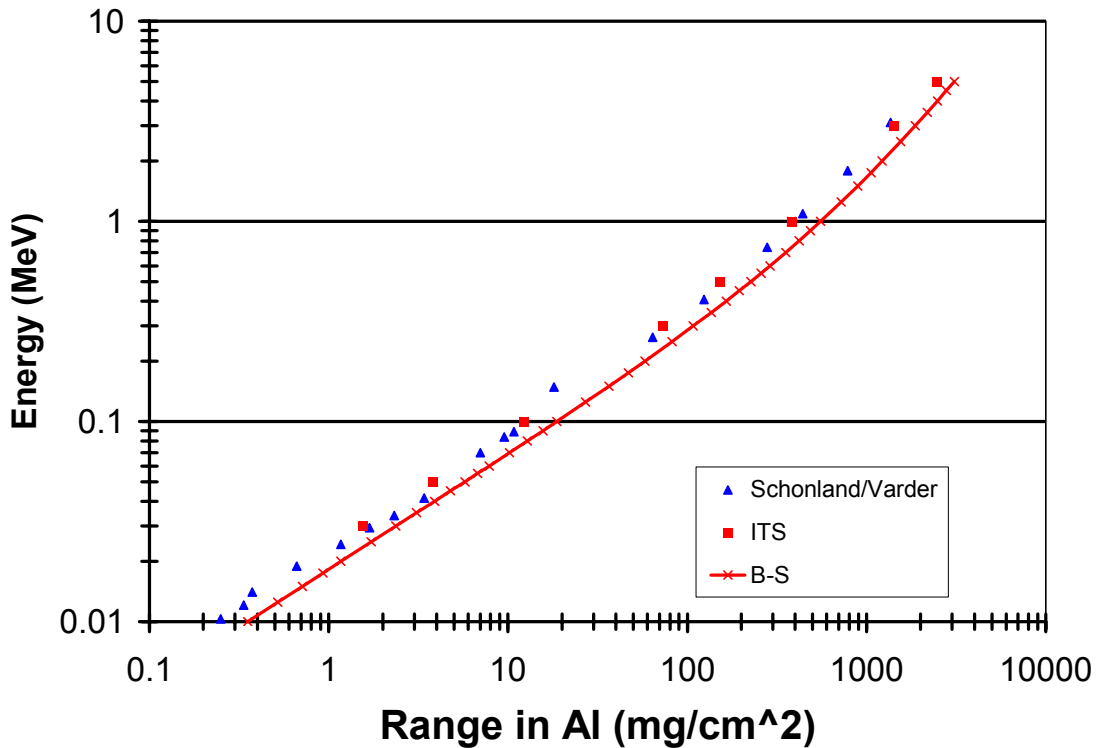

Fig. A2. Extrapolated range calculations of ITS 3.0 compared to experimental data from Schonland and Varder and the Berger-Seltzer Continuous Slowing Down Approximation range (total path length).
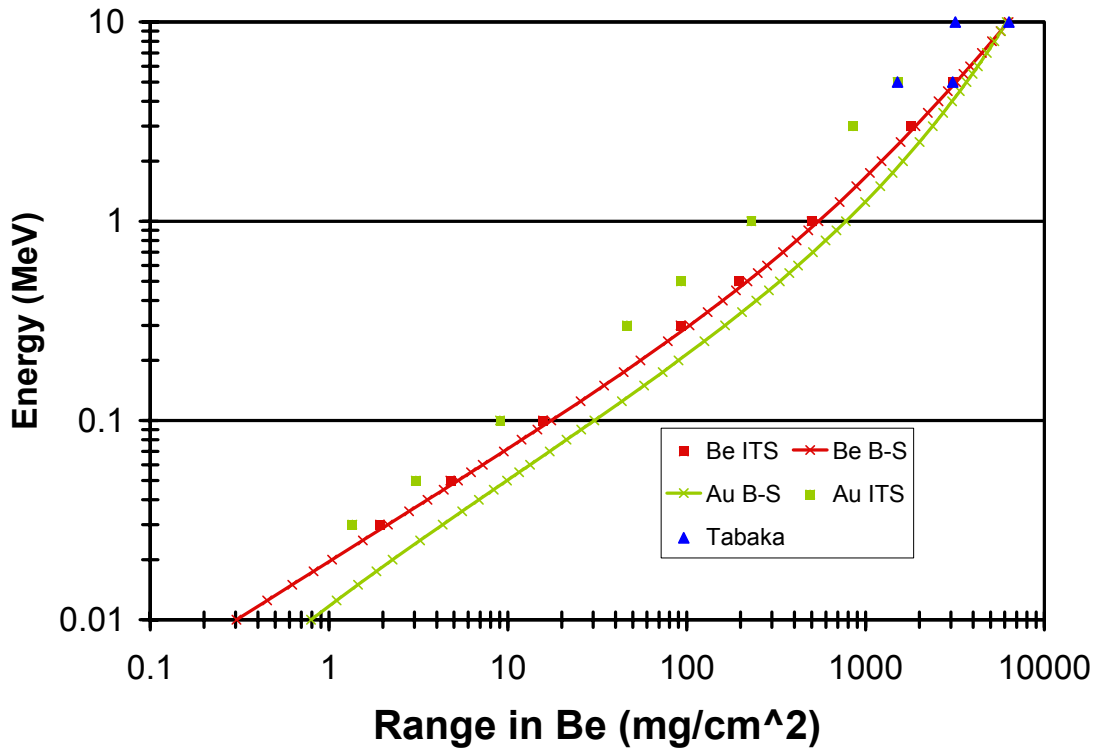
Fig. A3. ITS simulations for beryllium and gold compared to experimental data from Tabata and the Continuous Slowing Down Approximation range. We see that as scattering is less important in lower Z materials, the extrapolated range approaches the CSDA range.
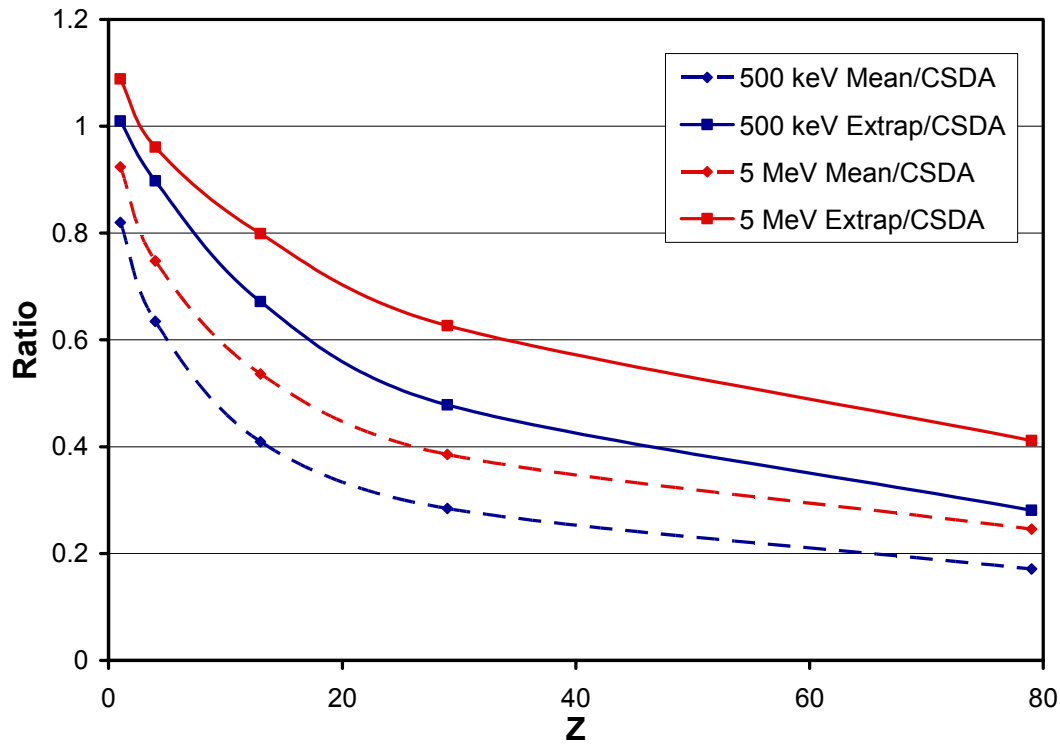
Fig. A4. The increase in the importance of scattering with increasing Z is depicted by the falloff in the mean range/CSDA and the extrapolated range/CSDA ratios. As expected, the effect of scattering is lower for higher energy particles. The dip above 1 for Z=1 is probably due to small errors introduced into the linear interpolation of the extrapolated range.

[1] T. Tabata, P. Andreo, and R. Ito, *Atomic Data and Nuclear Data Tables*, **56**, 105-131 (1994)
[2] T. Tabata, P. Andreo, K. Shinoda, and R. Ito, *Nucl. Instrum. Methods Phys. Res. B*, **vol. 95**, pp. 289–299, 1995.

[3] T. Tabata, P. Andreo, K. Shinoda, and R. Ito, *Nucl. Instrum. Methods Phys. Res. B,* **vol. 108**, pp. 11-17, 1996.
[4] R. D. Evans. "The Atomic Nucleus", (Robert E. Krieger Publishing Company, Inc. Malabar, Florida, 1955).
[5] B. F. J. Schonland, *Proc. Roy. Soc. (London)*, **A108**: 187, 1925.
[6] R. W. Varder, *Phil. Mag.*, **29**: 725 (1915).